ChemCatChem

Research Article
doi.org/10.1002/cctc.202301077

Chemistry Europe
European Chemical Societies Publishing

www.chemcatchem.org

Ultrasmall Cu Nanoparticles Supported on Crystalline, Mesoporous ZnO for Selective CO_2 Hydrogenation

Mingzhen Hu[+],[a] Xingxu Lu[+],[b] Chunxiang Zhu,[b] Tiangang Yang,[a] Haiyan Tan,*[c] Lei Jin,[a] Peter Kerns,[a] Michael Meng,[a] Steven L. Suib,[a, b, c] Puxian Gao,*[b, c] and Jie He*[a, c]

Converting CO_2 to value-added chemicals, *e. g.*, CH_3OH, is highly desirable in terms of the carbon cycling while reducing CO_2 emission from fossil fuel combustion. Cu-based nanocatalysts are among the most efficient for selective CO_2-to-CH_3OH transformation; this conversion, however, suffers from low reactivity especially in the thermodynamically favored low temperature range. We herein report ultrasmall copper (Cu) nanocatalysts supported on crystalline, mesoporous zinc oxide nanoplate (Cu@*m*ZnO) with notable activity and selectivity of CO_2-to-CH_3OH in the low temperature range of 200–250 °C. Cu@*m*ZnO nanoplates are prepared based on the crystal-crystal transition of mixed Cu and Zn basic carbonates to mesoporous metal oxides and subsequent hydrogen reduction. Under the nanoconfinement of mesopores in crystalline ZnO frameworks, ultrasmall Cu nanoparticles with an average diameter of 2.5 nm are produced. Cu@*m*ZnO catalysts have a peak CH_3OH formation rate of 1.13 $molh^{-1}$ per 1 kg under ambient pressure at 246 °C, about 25 °C lower as compared to that of the benchmark catalyst of Cu-Zn-Al oxides. Our new synthetic strategy sheds some valuable insights into the design of porous catalysts for the important conversion of CO_2-to-CH_3OH.

Introduction

CO_2 in atmosphere (> 410 ppm in 2021) has raised great global concerns on the climate change.[1–4] The keys to warding off fast increase of atmospheric CO_2 lie in developing clean energy to substitute fossil fuels as the main source of CO_2 production and, more importantly, facilitating efficient CO_2 conversion especially through catalysis.[5–7] In this regard, capturing CO_2 from massive fossil fuel combustion and further selectively converting it to more valuable fuels, *e. g.*, CH_3OH, by reacting with renewable hydrogen is one of the most promising routes.[8–10] Cu-based catalysts such as the state-of-the-art Cu-Zn-Al oxides have shown great potentials in catalyzing selective hydrogenation of CO_2 to CH_3OH but they still suffer from low efficiency especially under low reaction temperatures.[11–13]

Thermodynamic insights into CH_3OH formation through selective hydrogenation of CO_2 suggest that the CO_2-to-CH_3OH transformation is exothermic with the volume reduction as displayed in eq 1.[14] Therefore, high pressure and low temperature would favor the formation of CH_3OH. On the other hand, CO_2 is chemically inert, and the increase of reaction temperature is generally essential to promote its activation and conversion. However, increasing reaction temperature also promotes the competitive endothermic CO_2-to-CO transformation that is known as the reverse-water-gas-shift (RWGS) reaction as shown in eq 2.[15]

$$CO_2 + 3H_2 \rightleftharpoons CH_3OH + H_2O \quad \Delta H_{298K} = -49.5\ kJmol^{-1} \quad (1)$$

$$CO_2 + H_2 \rightleftharpoons CO + H_2O \quad \Delta H_{298K} = 41.2\ kJmol^{-1} \quad (2)$$

As a result, the selectivity to CH_3OH is greatly hampered by the formation of CO under high reaction temperatures. Although balancing the trade-off between CO_2 conversion activity and CH_3OH selectivity is challenging, improving the reactivity of Cu-based catalysts at low temperature (below 250 °C) is highly desirable in terms of retaining a high selectivity to CH_3OH. To this end, a series of strategies including the chemical modification of support and the modulation of additives have been explored previously.[16–18] For example, the Lewis acidic Zr sites in $Cu/ZrO_2/SiO_2$ were found effective to stabilize formate and methoxy intermediates than Cu/SiO_2 without acidic promoters.[19] Surface defects of the oxide support, *e. g.*, oxygen vacancies, also accelerated CO_2 conversion by facilitating the redox kinetics in CO_2 activation.[20,21] However, because of the reaction complexity and difficulty in capturing intermediates during reaction, the CH_3OH formation mechanism over Cu-based catalysts is still on debate. For example, both CuZn alloy and Cu/ZnO interface have been proposed to be the

[a] *Dr. M. Hu,[+] T. Yang, L. Jin, P. Kerns, M. Meng, Prof. S. L. Suib, Prof. J. He*
Department of Chemistry
University of Connecticut
Storrs, Connecticut 06269 (USA)
E-mail: jie.he@uconn.edu

[b] *Dr. X. Lu,[+] C. Zhu, Prof. S. L. Suib, Prof. P. Gao*
Department of Materials Science and Engineering
University of Connecticut
Storrs, Connecticut 06269 (USA)
E-mail: puxian.gao@uconn.edu

[c] *Dr. H. Tan, Prof. S. L. Suib, Prof. P. Gao, Prof. J. He*
Institute of Materials Science
University of Connecticut
Storrs, Connecticut 06269 (USA)
E-mail: haiyan.tan@uconn.edu
jie.he@uconn.edu

[+] *These authors contributed equally to this work.*

Supporting information for this article is available on the WWW under https://doi.org/10.1002/cctc.202301077

active sites for CH_3OH formation.[21–25] When Zn/Cu(111) was gradually oxidized to ZnO/Cu(111), the formation rate of CH_3OH obviously increased, indicating that the ZnO/Cu interface is the active site for CH_3OH formation.[24] However, Sehested et al. demonstrated that there was a strong interdependency of the methanol formation activity and CuZn contents using H_2-TPD characterizations.[23] In operando X-ray absorption spectroscopy, metallic Zn species in the form of CuZn alloy was beneficial for CH_3OH formation; but the CuZn alloy was found to be unstable under reaction conditions.[26,27] Nevertheless, the common agreement is that small Cu nanoparticles with rich surface-exposed corner and edge sites are beneficial for activating CO_2 and enhancing low temperature CO_2-to-CH_3OH conversions.[28,29] Thus, synthesis of ultrasmall Cu nanoparticles with metallic Zn modification is expected to improve the formation rate and the selectivity to CH_3OH at lower temperatures. On the other hand, precise preparation of the highly efficient CO_2-to-CH_3OH conversion catalyst integrated with ultrafine Cu nanoparticles on a mass-transfer-favored support (e. g., porous oxides) is very challenging, which commonly requires complex synthetic procedures.

Herein, using a crystal-crystal transition strategy as we developed recently,[30–34] we can grow and stabilize ultrasmall Cu nanoparticles within highly crystalline mesoporous ZnO (*m*ZnO) support. With single-crystalline basic carbonates synthesized via a hydrothermal method, porous transition metal oxides with highly crystalline frameworks can be synthesized through the thermal conversion of hydroxide carbonates to oxides. The removal of small molecules, like CO_2 and water can thus template the in-situ formation of mesopores. Crystalline mesoporous transition metal oxides can not only serve as a support with favorable mass transfer channels but also provide powerful nanoconfinement to grow and stabilize ultrasmall metal nanoparticles. The Cu@*m*ZnO catalysts with favorable porous frame and intriguing synergy from metallic Zn components formed by virtue of the strong metal-support interactions can efficiently enhance the selectivity to CH_3OH than that of the benchmark Cu-Zn-Al oxides in a much lower temperature. Our method likely opens a new opportunity to develop new catalysts for efficient CO_2-to-CH_3OH conversion.

Results and Discussion

Figure 1a shows the schematic preparation process of Cu@*m*ZnO. The loading amount of Cu was controlled as the feeding ratio of copper nitrate relative to zinc nitrate with a ratio of 1 wt%, 5 wt% and 10 wt% of Cu loading on *m*ZnO were prepared. The samples were designated as Cu@*m*ZnO-X, where the X represented the loading amount of Cu. To prepare Cu@*m*ZnO-5, mixed Cu and Zn basic carbonates were prepared through solvothermal synthesis in tetraethylene glycol (TEG) and water. Through a thermal calcination at 300 °C under air, mesoporous mixed oxides were obtained (see synthetic details in supporting information). Metallic Cu was formed by a hydrogen reduction at 250 °C. The formation of hydrozincite $Zn_4CO_3(OH)_6 \cdot H_2O$ (JCPDS 11-0287) was confirmed by X-ray

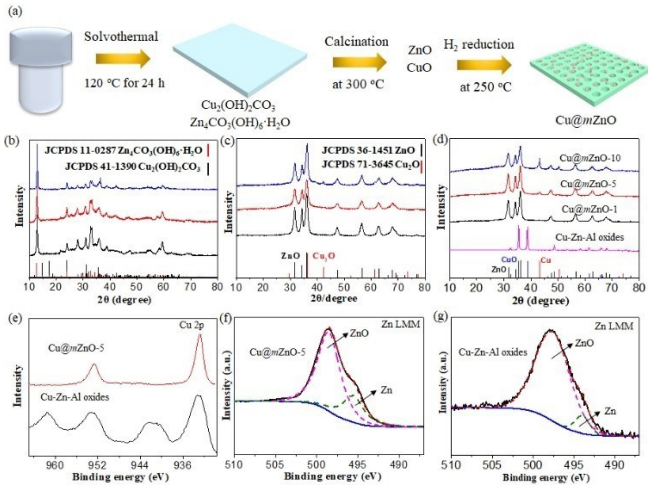

Figure 1. (a) Synthetic scheme of mesoporous Cu@*m*ZnO-5. (b) XRD patterns of mixed Cu and Zn basic carbonates of $Cu_2(OH)_2CO_3$ and $Zn_4CO_3(OH)_6 \cdot H_2O$. (c) XRD patterns of the calcined products at 300 °C in air for 3 h. (d) XRD patterns of mesoporous Cu@*m*ZnO-5 after H_2 reduction at 250 °C for 2 h and Cu–Zn–Al oxides. (e) Cu 2p XPS spectra of Cu@*m*ZnO-5 and Cu-Zn-Al oxides. (f,g) Zn LMM Auger spectra of (f) Cu@*m*ZnO-5 and (g) Cu-Zn-Al oxides.

diffraction (XRD) as shown in Figure 1b. In all three different loadings, the most common form of cooper hydroxide carbonate $Cu_2(OH)_2CO_3$ (JCPDS 41-1390) as a minor phase did not show obvious peaks. Thermogravimetric analysis (TGA) in Figure S1 reveals that $Zn_4CO_3(OH)_6 \cdot H_2O$ with a 1 wt% of Cu loading has sharply decomposed around 300 °C with a weight loss of ~27 wt %. This value is close to the theoretical decomposition weight loss of $Zn_4CO_3(OH)_6 \cdot H_2O$, ~26.7 wt%. With a higher Cu loading, the mixed phases had a clear shoulder peak appearing at 316 °C, assigned to the thermal decomposition temperature of $Cu_2(OH)_2CO_3$. The copper and zinc basic carbonates transformed to mesoporous metal oxides by releasing small gas molecules such as CO_2 and H_2O. ZnO phase (JCPDS 36-1451) was confirmed by XRD as displayed in Figure 1c. While the XRD peaks of CuO (002) and (111) heavily overlapped with ZnO, we note that a significant amount of Cu_2O was seen in the XRD patterns for Cu@*m*ZnO-10 (Figure 1c), likely thermally reduced by residual surface ligands. After hydrogen reduction at 250 °C for 2 h, the formation of Cu nanoparticles was confirmed by XRD shown in Figure 1d. The XRD peak at $2\theta = 43°$ is assigned to the (111) plane of metallic fcc Cu (JCPDS 04-0836). For Cu@*m*ZnO-5, the Zn-to-Cu ratio is approximately 21 with a molar ratio of Cu to ZnO of 1 : 4.7, slightly smaller than the feeding ratio of Cu to Zn, 1 : 6.4 (mol) as determined by energy-dispersive X-ray spectroscopy (EDS) analysis.

From high-resolution X-ray photoelectron spectroscopy (XPS) in Figure 1e, Cu 2p shows the Cu $2p_{3/2}$ and Cu $2p_{1/2}$ peaks of Cu@*m*ZnO-5 at 932.8 eV and 952.6 eV, respectively, which agrees well with metallic Cu as reported previously.[35] By comparison, under the same reduction conditions, Cu components of Cu-Zn-Al oxides are in the form of CuO (JCPDS 48-1548) as suggested by XRD characterizations in Figure 1d. Cu

2p XPS results display that the Cu $2p_{3/2}$ and Cu $2p_{1/2}$ binding energy peaks of Cu in Cu-Zn-Al oxides are centered at 933.1 eV and 953.4 eV that are well in line with that of CuO.[36,37] The intensified satellite peaks at around 941.8 eV and 961.5 eV of Cu-Zn-Al oxides are also characteristic of CuO for Cu-Zn-Al oxides.[37] To investigate the chemical states of surface Zn in Cu@*m*ZnO-5 and Cu-Zn-Al oxides, the Zn LMM Auger peak is used due to the heavy overlap of Zn 2p peaks between metallic Zn and ZnO.[38] As shown in Figure 1f, the Zn LMM peak shows the main peak centered at 498.5 eV, assigned to Zn^{2+} cations in ZnO. There is a clear shoulder peak at 495.5 eV from the metallic Zn.[25] The ratio of metallic Zn to Zn^{2+} cations is estimated to be 1 : 3 (mol) based on the Zn LMM Auger area. By contrast, the ratio of metallic Zn to Zn^{2+} in Cu-Zn-Al oxides was about 1 : 12 (Figure 1g), much lower than that of Cu@*m*ZnO-5 (1 : 3, Figure 1f).[25]

Figure 2 shows the scanning transmission electron microscopy (STEM) characterizations of Cu@*m*ZnO-5. As a control, the STEM image of mixed Cu and Zn basic carbonates is given in Figure 2a. The mixed basic carbonates appeared as two-dimensional nanosheets and their lateral size is not uniform with lengths up to micrometers. Similar results were also identified for Cu@*m*ZnO-1, Cu@*m*ZnO-10 and pure *m*ZnO, wherein all catalysts showed two-dimensional nanosheet-like morphology with irregular porous structures as summarized in Figure S2. Those nanosheets are single-crystalline as confirmed by selected area electron diffraction (SAED) (Figure 2b) and they did not show any porosity. However, they were sensitive to the electron beam. With a high beam dose, nanosheets would be damaged to form porous structures. For Cu@*m*ZnO-5, *m*ZnO with its crystalline structures confirmed by XRD (Figure 1c) appeared to be mesoporous and the structural integrates were highly preserved (Figure 2c). The crystal-to-crystal transition retained the high crystallinity of ZnO frameworks while releasing CO_2 and H_2O as suggested previously.[30] The high-angle annular dark-field STEM (HAADF-STEM) image in Figure 2d shows that ultrasmall Cu nanoparticles are homogeneously dispersed on mesoporous ZnO nanosheets. The average size of Cu nanoparticles is measured to be 2.5 ± 0.5 nm as displayed in Figure 2e. The pores are non-spherical and some of them are elongated in the size range of 3–8 nm. The cross-section STEM in Figure 2f shows the thickness of nanosheets, ~20 nm. The Brunauer-Emmett-Teller (BET) specific surface area of Cu@*m*ZnO-5 was measured to be 61.6 m^2/g by N_2 adsorption-desorption isotherms. We note that the weak Type-IV hysteresis of Cu@*m*ZnO catalysts was derived from their small BET specific surface areas as summarized in Table S1. To further confirm the porous structure of Cu@*m*ZnO, we have performed careful transmission electron microscopy. As given in Figure S2, Cu@*m*ZnO-1, Cu@*m*ZnO-5, and Cu@*m*ZnO-10 showed obvious mesopores within their two-dimensional nanosheet-like skeletons. In addition, as for pure *m*ZnO support, the mesoporous structures were also clearly identified on its two-dimensional nanosheet skeleton. As displayed in Figure S3, a representative isotherm of Cu@*m*ZnO-5 is identified with an average pore size of 6.5 nm (Table S1), which agrees well with the value obtained from the dark-field STEM measurements in Figure 2d–e. Note that, the miscibility of single-crystalline-like basic carbonates was very limited. A high Cu loading would result in the phase segregation. For Cu@*m*ZnO-10, Cu with clustering and sintering appeared to be less uniform on *m*ZnO (see Figure S4).

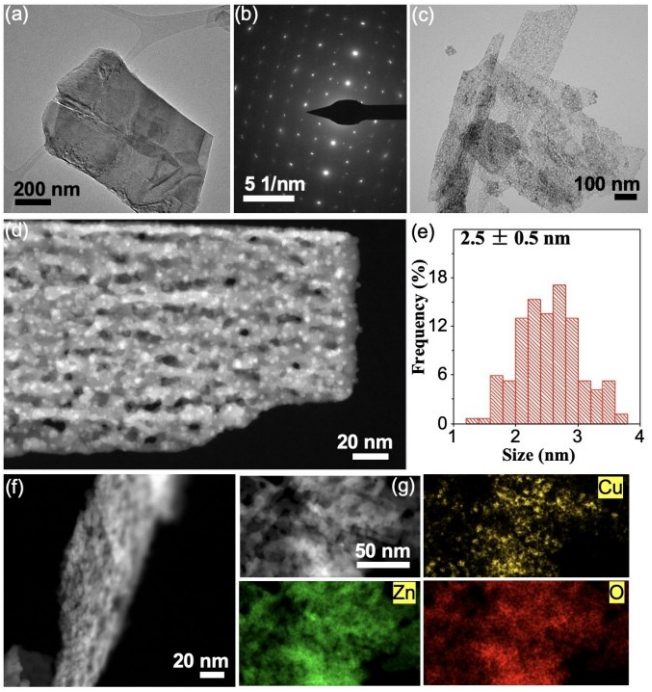

Figure 2. Characterization of Cu@*m*ZnO-5. (a) STEM image and (b) selected-area electron diffraction of mixed Cu and Zn basic carbonates. (c) STEM and (d) aberration-corrected HAADF-STEM of Cu@*m*ZnO-5. (e) Average Cu particle size and distribution on Cu@*m*ZnO-5 from STEM measurement. (f) STEM image of Cu@*m*ZnO-5 under a tilted view. (g) corresponding EDS mapping images of Cu@*m*ZnO-5.

CO_2 hydrogenation with different Cu@*m*ZnO catalysts was conducted using the benchmark Cu-Zn-Al oxides as a control. The catalytic evaluation was carried out in a fixed-bed quartz tubular reactor. To do so, 50 mg of the catalyst was firstly pretreated with H_2 with a flow rate of 75 SCCM (standard cubic centimeters per minute) at 250 °C for 2 h. The reactant gas mixture (25 vol % CO_2 and 75 vol% H_2) was passed through the reactor at a space velocity of 47,750 h^{-1}. The composition of the gas products was analyzed online using pre-calibrated FT-IR spectrometer. Figure 3a shows the methanol formation rate highly depends on the Cu loadings of Cu@*m*ZnO. All Cu@*m*ZnO catalysts with different Cu loadings were efficient to activate CO_2 to CH_3OH as displayed in Figure S5. The reactivity, as the methanol formation rate plotted against temperature, had a typical volcano shape, where the maximum methanol formation rates of 1.08 and 1.13 $molh^{-1}$ kg^{-1} appeared at 246 °C for Cu@*m*ZnO-10 and Cu@*m*ZnO-5, respectively. Cu@*m*ZnO-1 showed a maximum methanol formation rate of 0.16 mol h^{-1} kg^{-1} at 271 °C due to its low Cu loading, which likely did not have enough active sites for CO_2 activation. At a lower space velocity of 19100 h^{-1}, the Cu@*m*ZnO-5 catalyst still exhibited a lower maximum methanol formation rate of 0.36 mol h^{-1} kg^{-1} at 246 °C shown in Figure S6. The higher methanol formation rate over the Cu@*m*ZnO-5 catalyst with a

Research Article
doi.org/10.1002/cctc.202301077
Chemistry Europe
European Chemical Societies Publishing

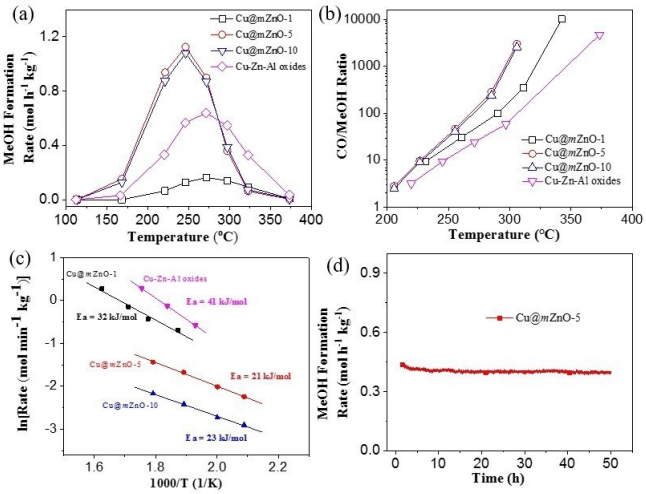

Figure 3. CO_2 hydrogenation summary and comparison (a) CH_3OH formation rate. (b) CO-to-CH_3OH ratios of Cu@*m*ZnO and Cu-Zn-Al oxides as a function of reaction temperature, respectively. (c) Arrhenius plots for CO_2 conversion over Cu@*m*ZnO and Cu-Zn-Al oxides catalysts. (d) Methanol formation rate stability test over the Cu@mZnO-5 for 48 h under 246 °C, 1 bar. The stability test was conducted at a lower space velocity of 19100 h^{-1}, while the other samples were tested at a higher space velocity of 47,750 h^{-1}.

higher space velocity indicates the excellent mass transfer efficiency of the catalyst, endowed by its rich mesoporosity. Cu@*m*ZnO-10 had similar reactivity and product selectivity (Figure 3b). A lower CH_3OH formation rate at a higher temperature is due to the thermodynamic competition of the two products of CO and CH_3OH. The formation of CH_3OH is exothermic, and therefore, favored thermodynamically under a lower temperature as aforementioned. The increase of reaction temperature would increase the formation rate of both CO and CH_3OH by promoting CO_2 activation and conversion. However, the CO formation through the RWGS reaction is endothermic, and it becomes dominated under high temperature where the selectivity to CH_3OH is lower (Figure 3b). Compared with Cu@*m*ZnO-5, the Cu-Zn-Al oxides showed a similar volcano-shaped trend with the highest CH_3OH formation rate of 0.64 mol h^{-1} kg^{-1} catalyst obtained at 271 °C. As such, the Cu@*m*ZnO-5 displayed a 25 °C lower peak temperature and ca. 2 times higher CH_3OH formation rate, as compared to the state-of-the-art Cu-Zn-Al oxides.

CO_2 hydrogenation activity is highly dependent on the average size of Cu. With ultrasmall Cu particles below 3 nm, a large number of low-coordinated Cu sites allow the hydrogen spillover to form Cu-H bonds at the edge/corner sites,[39] improving the reactivity of CO_2 hydrogenation. With larger Cu particles, many Cu surface sites become unavailable for the reaction, lowering the overall catalytic activity. The peak CH_3OH formation rate of Cu@*m*ZnO-5 is 1.13 $molh^{-1}$ per 1 kg of catalyst at 246 °C. The peak activity of Cu-Zn-Al oxides is 0.64 mol h^{-1} per 1 kg of catalyst at 271 °C, about 1/2 of Cu@*m*ZnO-5, indicating the excellent low temperature activity for CO_2-to-CH_3OH conversion of the Cu@*m*ZnO-5. Table 1 summarizes the activity comparison of reported Cu-based catalysts. Cu@*m*ZnO-5 is among the best catalysts to produce methanol under ambient pressure and low temperature. To be noted, the scope of this work is to formulate a high active catalyst for selective hydrogenation of CO_2 to CH_3OH at a low temperature and pressure and no high-pressure testing was conducted.

Figure 3b shows the CO-to-CH_3OH ratios of Cu@*m*ZnO catalysts and Cu-Zn-Al oxides as a function of reaction temperature. The CO-to-CH_3OH ratio of Cu@*m*ZnO is much greater than that of Cu-Zn-Al oxides throughout the temperature range from 200 °C to 375 °C. Figure 3c exhibits the Arrhenius plot on the CO_2 conversion rate against the reciprocal of temperature. The apparent activation energy (E_a), determined from the slopes of the Arrhenius plot, is 21 and 41 kJ · mol^{-1} for Cu@*m*ZnO-5 and Cu-Zn-Al oxides, respectively. The CO_2 activation energy over Cu@*m*ZnO-5 is 20 kJ · mol^{-1} lower than that over Cu-Zn-Al oxides. On the other hand, the activation energy value of the Cu@*m*ZnO-1 catalyst (32 kJ · mol^{-1}) was markedly larger than that of Cu@*m*ZnO-5 and Cu@*m*ZnO-10 catalysts, which possibly derived from the fact that Cu was primarily in the form of highly reactive metallic state[40] in the Cu@*m*ZnO-5 and the Cu@*m*ZnO-10 catalysts while Cu was in the form of less reactive oxidized state in Cu@*m*ZnO-1 as displayed in Figure S7. Despite a higher Cu loading of Cu@*m*ZnO-10, its catalytic activity was comparable to that of Cu@*m*ZnO-5, which possibly derived from the poor dispersity of Cu nanoparticles as shown in Figure S4.

Table 1. Reactivity of reported catalysts for the MeOH formation rate comparison with Cu@*m*ZnO-5.

Entry	CH_3OH formation rate ($molh^{-1}$ per 1 kg of catalyst)	Temperature (°C)	Pressure (MPa)	Reference
Cu@mZnO-5	1.13	246	0.1	Current work
Cu@LaO_x	~2.03	240	3.0	*Appl. Catal. B*, 2019, 251, 119
CuO/ZnO/Al_2O_3-U-1	0.682	240	3.0	*Fuel*, 2016, 164, 191–198
20%CuZn/rGO	1.02	250	1.5	*CO_2 Util*, 2016, 16, 104–113
Cu/ZnO/ZrO_2-0	4.34	230	5.0	*Appl. Catal. B*, 2016, 191, 8–17
Cu-ZnO/TiO_2-ZrO_2	1.64	240	3.0	*Appl. Surf. Sci*, 2015, 338, 146–153
Cu-Zn/SiO_2	2.02	250	2.0	*Appl. Catal. B*, 2001, 29, 207–215
Cu-Zn-Al/ZnO nanorod array	1.4	200	0.1	*Adv. Mater. Interfaces* 2018, 5, 1700730.

We further examined the stability of Cu@*m*ZnO catalysts. The on-stream catalytic stability measurement of Cu@*m*ZnO-5 carried out at 246 °C at a lower space velocity of 19100 h^{-1} is plotted in Figures 3d and S5. During the catalytic evaluations, we used a different GHSV (19100 h^{-1} instead of 47750 h^{-1}). To make it clear, in evaluating the activity of investigated catalyst, a high GHSV (47750 h^{-1}) was selected with the aim of assuring the reaction occurrence at a kinetics region to reflect the intrinsic activity of the catalyst. A low GHSV (19100 h^{-1}) was used to examine stability to attain high conversion of reactants for practical applications. With 48 h testing at 246 °C, the CH_3OH formation rate remained around 0.39 mol h^{-1} per 1 kg of catalyst, which agreed well with temperature-dependent formation rate plotted in Figures S6. In the meanwhile, the CO-to-CH_3OH ratio and the CO formation rate (Figure S8) were also very stable with minimum changes. Further electron microscopy characterizations of post-reaction Cu@*m*ZnO-5 are given in Figure S9. The spent Cu@*m*ZnO-5 catalyst remained stable after stability measurement, and the structural integrity of porous frameworks was largely retained.

The reaction mechanism of selective hydrogenation of CO_2 to CH_3OH over Cu-based catalysts is still controversial where both the CuZn alloy and the Cu/ZnO interface are claimed to be the active sites to activate CO_2 molecules. The electronic interaction between ZnO and Cu contributes largely to the high selectivity of CO_2 to CH_3OH. Temperature-programmed reduction with hydrogen (H_2-TPR) analysis was used to detect the reducibility of Cu@*m*ZnO-5 and Cu-Zn-Al oxides, respectively. As given in Figure S10, the reduction peaks of Cu@*m*ZnO shifted obviously to lower temperatures in comparison with that of Cu-Zn-Al oxides, suggesting easy reducibility of surface oxygen species on the Cu@*m*ZnO-5. This is likely due to the stronger metal-support interaction between ultrasmall Cu particles (and metallic Zn) and surface oxygen species. The strong metal-support interaction not only endows Cu@*m*ZnO-5 with enhanced H_2 activation ability, but also promotes partial reduction of mesoporous ZnO to Zn species as shown by the Zn LMM characterizations in Figure 1f. The metallic Zn promoting effect has been previously revealed on Cu-based catalyst in selective hydrogenation of CO_2 to CH_3OH.[26] The introduction of Zn metal was found effectively to stabilize formate species that were identified as the rate-determining step of methanol formation. As discussed in Figure 1f and g, the Zn to ZnO ratio of Cu@*m*ZnO-5 is calculated to be about 1 : 3, in good consistence with strong metal-support interaction. By comparison, less metallic Zn component was identified in the Cu-Zn-Al oxides. The larger amount of Zn contents of Cu@*m*ZnO seems of great importance in attaining a higher methanol formation rate than that of Cu-Zn-Al oxides. The enrichment of the metallic Zn component in the Cu@*m*ZnO-5 catalyst could be served as intuitive evidence that contributes to the different catalytic performance between Cu@*m*ZnO-5 and Cu-Zn-Al oxides, although we did not have in situ results on the structural evolution of metallic Zn under reaction conditions. Moreover, the Cu@*m*ZnO-5 catalyst was also one of the most efficient and stable CO_2-to-CH_3OH conversion catalysts in comparison with previous results as summarized in Table 1.

Conclusions

To summarize, we demonstrated the facile preparation of crystalline, mesoporous ZnO supported ultrasmall Cu particles by using a template-free, crystal-to-crystal transition method. The synthesis is based on the crystal-to-crystal transformation from mixed Cu and Zn basic carbonates to mesoporous metal oxides at a low temperature (300 °C). The release of small molecules like CO_2 and H_2O led to the formation of well-defined mesopores within the nanoplates skeleton. After hydrogen reduction at 250 °C, ultrasmall Cu particles of 2.5 ± 0.5 nm were produced as a result of the nanoconfinement by mesoporous ZnO frameworks. Cu@*m*ZnO catalysts exhibited a much lower reaction temperature, as large as 25 °C, to maximize CO_2-to-CH_3OH formation rate, as compared to Cu-Zn-Al oxides. Given the ultrasmall Cu particles and the strong metal-support interaction in the porous framework, Cu@*m*ZnO catalysts are among the most active and selective catalysts to produce CH_3OH through CO_2 hydrogenation. Our results are expected to provide a new approach for rational design of highly efficient catalysts for low-temperature CO_2 activation.

Experimental

Chemicals and Materials

All chemicals were of analytical grade and used as received without further purification. Copper(II) nitrate trihydrate, zinc(II) nitrate hexahydrate, urea and TEG were purchased from Sigma-Aldrich. Deionized water (High-Q, Inc. 103S Stills) with a resistivity of > 10.0 MΩ was used in all experiments.

Preparation of mesoporous Cu@mZnO

30 mL of tetraethylene glycol (TEG) and 30 mL of water were mixed together to make a homogeneous solution. 0.6 g of urea, 5 mmol of zinc(II) nitrate hexahydrate (1.49 g), and 0.32 mmol of copper(II) nitrate trihydrate (0.076 g) were then added to the above solvent and stirred for 1 h at room temperature to fully dissolve the two salts. The solution was then transferred into a Teflon lined stainless steel autoclave, sealed and maintained at 120 °C for 12 h. After the reactor was cooled to room temperature, the products were readily obtained by centrifugation. The final product was sufficiently washed by water and ethanol for three times and then allowed for drying at 40 °C under vacuum overnight. Those mixed basic carbonates were calcined at 300 °C for 3 h in air and followed by reduced by hydrogen at 250 °C for 2 h to produce Cu@*m*ZnO. The loading amount of Cu was controlled as the feeding ratio of copper nitrate with a ratio of 1 wt %, 5 wt% and 10 wt % relative to zinc nitrate. The samples were denoted as Cu@*m*ZnO–X, where the X represents the loading amount of Cu. The benchmark catalyst of Cu–Zn–Al oxides was also prepared according to a previous report as our control.[41]

Catalytic evaluations

The catalytic activity of Cu@*m*ZnO and Cu–Zn-Al oxides toward selective hydrogenation of CO_2 was evaluated under atmospheric pressure in a continuous flow fixed-bed quartz tubular reactor. In a typical process, 50 mg of the catalyst was placed in the reactor. The

reactant gas mixture (25 vol % CO_2, and 75 vol % H_2) was passed through the reactor at a space velocity 47750 h^{-1}. The composition of the outlet gas was analyzed by gas chromatography. Before catalytic measurements, the catalyst was pretreatment by pure hydrogen with a flow rate of 75 cm^3 min^{-1} at 250 °C for 2 h. The products were analyzed by an online micro-GC 4900 and Fourier transform infrared spectrometer (Thermo Fisher Nicolet 6700, FT-IR) equipped with a gas cell. Methanol was quantified using FT-IR, while micro-GC was pre-calibrated with CO_2, CO, H_2, CH_4, and N_2.

The methanol production rate (R_{MeOH}) and selectivity (S_{MeOH}) were calculated as following.

$$R_{MeOH}\ (molkg^{-1}h^{-1}) = MFR_{methanol}/W_{catalyst}$$

$$S_{MeOH}\ (\%) = C_{methanol}/(\delta_{methanol} + C_{CO}) * 100\%$$

where $MFR_{methanol}$ is the molar flow rate of methanol, unit is mol/h. $W_{catalyst}$ is the weight of Cu@*m*ZnO loaded, unit is kg. $C_{methanol}$ is the concentration of methanol in ppm (parts per million) and C_{CO} is the concentration of carbon monoxide in ppm, respectively. For all testing, only CO and MeOH are detected as the products.

Characterizations

The crystallographic structures were analyzed by powder X-ray diffraction (XRD, Bruker D8 Focus X-ray diffractometer, Cu Kα radiation, $\lambda = 0.1542$ nm). X-ray photoelectron spectroscopy (XPS) analysis was conducted on ESCALAB 250 Xi X-ray photoelectron spectrometer with Al Kα radiation. The specific surface area measurement was conducted on a Quantachromeautosorb IQ_2 instrument (Quantachrome Instruments). Transmission electron microscopy (TEM) analysis and in-situ heating STEM was carried out on Talos F200X FEG TEM/STEM operating at 200 kV. Elemental mappings were collected with Super X system equipped with 4 Silicon Drift Detectors offering a total collection angle of 0.9 srad. The high-resolution STEM images were collected via Titan Themis 60–300 equipped with a probe corrector to correct condenser lens aberration leading to 0.08 nm spatial resolution at 300 kV. H_2-TPR was conducted by loading 50 mg of sample in a U shape reactor. Before measurements, the sample was firstly annealed under Ar at 300 °C for 2 h and H_2 was then switched on. The temperature was gradually increased to 650 °C, during which the data was collected as function of temperature.

Supporting Information

Synthetic details of Cu@*m*ZnO catalysts, and more analysis results on XRD, TGA, H_2-TPR, STEM images, BET and stability.

Acknowledgements

J.H. is grateful for financial support from the National Science Foundation (CBET-1705566). P.-X.G. thanks for the financial support from the US Department of Energy (DE-EE0008423). The SEM/TEM studies were performed using the facilities in the UConn/Thermo Fisher Scientific Center for Advanced Microscopy and Materials Analysis (CAMMA).

Conflict of Interests

The authors declare no conflict of interest.

Data Availability Statement

The data that support the findings of this study are available from the corresponding author upon reasonable request.

Keywords: Porous crystalline oxides · basic carbonates · porous ZnO · CO_2 hydrogenation · methanol synthesis

[1] T. R. Karl, K. E. Trenberth, *Science* **2003**, *302*, 1719–1723.
[2] M. Aresta, *Carbon dioxide as chemical feedstock*, John Wiley & Sons **2010.**
[3] S. Bilgen, *Renewable Sustainable Energy Rev.* **2014**, *38*, 890–902.
[4] S. N. Riduan, Y. Zhang, *Dalton Trans.* **2010**, *39*, 3347–3357.
[5] X. Xiaoding, J. A. Moulijn, *Energy Fuels* **1996**, *10*, 305–325.
[6] A. Álvarez, A. Bansode, A. Urakawa, A. V. Bavykina, T. A. Wezendonk, M. Makkee, J. Gascon, F. Kapteijn, *Chem. Rev.* **2017**, *117*, 9804–9838.
[7] W. Wang, S. Wang, X. Ma, J. Gong, *Chem. Soc. Rev.* **2011**, *40*, 3703–3727.
[8] L. C. Grabow, M. Mavrikakis, *ACS Catal.* **2011**, *1*, 365–384.
[9] R. W. Dorner, D. R. Hardy, F. W. Williams, H. D. Willauer, *Energy Environ. Sci.* **2010**, *3*, 884–890.
[10] G. A. Olah, G. K. S. Prakash, A. Goeppert, *J. Am. Chem. Soc.* **2011**, *133*, 12881–12898.
[11] F. Studt, M. Behrens, E. L. Kunkes, N. Thomas, S. Zander, A. Tarasov, J. Schumann, E. Frei, J. B. Varley, F. Abild-Pedersen, J. K. Nørskov, R. Schlögl, *ChemCatChem* **2015**, *7*, 1105–1111.
[12] F. Liao, Y. Huang, J. Ge, W. Zheng, K. Tedsree, P. Collier, X. Hong, S. C. Tsang, *Angew. Chem. Int. Ed.* **2011**, *50*, 2162–2165.
[13] K. M. V. Bussche, G. F. Froment, *J. Catal.* **1996**, *161*, 1–10.
[14] O. Tursunov, L. Kustov, A. Kustov, *Oil Gas Sci. Technol. – Rev. d'IFP Energies Nouv.* **2017**, *72*, 30.
[15] J. Yoshihara, C. T. Campbell, *J. Catal.* **1996**, *161*, 776–782.
[16] A. Bansode, A. Urakawa, *J. Catal.* **2014**, *309*, 66–70.
[17] G. C. Chinchen, P. J. Denny, D. G. Parker, M. S. Spencer, D. A. Whan, *Appl. Catal.* **1987**, *30*, 333–338.
[18] E. Lam, K. Larmier, P. Wolf, S. Tada, O. V. Safonova, C. Copéret, *J. Am. Chem. Soc.* **2018**, *140*, 10530–10535.
[19] E. Lam, K. Larmier, P. Wolf, S. Tada, O. V. Safonova, C. Copéret, *J. Am. Chem. Soc.* **2018**, *140*, 10530–10535.
[20] C. M. Kalamaras, S. Americanou, A. M. Efstathiou, *J. Catal.* **2011**, *279*, 287–300.
[21] E. Lam, J. J. Corral-Pérez, K. Larmier, G. Noh, P. Wolf, A. Comas-Vives, A. Urakawa, C. Copéret, *Angew. Chem. Int. Ed.* **2019**, *131*, 14127–14134.
[22] M. Behrens, F. Studt, I. Kasatkin, S. Kühl, M. Hävecker, F. Abild-Pedersen, S. Zander, F. Girgsdies, P. Kurr, B.-L. Kniep, M. Tovar, R. W. Fischer, J. K. Nørskov, R. Schlögl, *Science* **2012**, *336*, 893–897.
[23] S. Kuld, M. Thorhauge, H. Falsig, C. F. Elkjær, S. Helveg, I. Chorkendorff, J. Sehested, *Science* **2016**, *352*, 969–974.
[24] S. Kattel, P. J. Ramírez, J. G. Chen, J. A. Rodriguez, P. Liu, *Science* **2017**, *355*, 1296–1299.
[25] S. Kuld, C. Conradsen, P. G. Moses, I. Chorkendorff, J. Sehested, *Angew. Chem. Int. Ed.* **2014**, *53*, 5941–5945.
[26] J. Nakamura, I. Nakamura, T. Uchijima, T. Watanabe, T. Fujitani, in *Studies in Surface Science and Catalysis*, eds. J. W. Hightower, W. Nicholas Delgass, E. Iglesia, A. T. Bell, Elsevier **1996**, vol. 101, pp. 1389–1399.
[27] A. Beck, M. Zabilskiy, M. A. Newton, O. Safonova, M. G. Willinger, J. A. van Bokhoven, *Nat. Catal.* **2021**, *4*, 488–497.
[28] X. Zhang, J.-X. Liu, B. Zijlstra, I. A. W. Filot, Z. Zhou, S. Sun, E. J. M. Hensen, *Nano Energy* **2018**, *43*, 200–209.
[29] J. Kleis, J. Greeley, N. A. Romero, V. A. Morozov, H. Falsig, A. H. Larsen, J. Lu, J. J. Mortensen, M. Dułak, K. S. Thygesen, J. K. Nørskov, K. W. Jacobsen, *Catal. Lett.* **2011**, *141*, 1067–1071.
[30] M. Hu, W. Yang, H. Tan, L. Jin, L. Zhang, P. Kerns, Y. Dang, S. Dissanayake, S. Schaefer, B. Liu, Y. Zhu, S. L. Suib, J. He, *Matter* **2020**, *2*, 1244–1259.

[31] Q. Luo, Z. Wei, H. Duan, L. Jin, R. N. T. Kankanamage, S. Shuster, S. L. Suib, J. F. Rusling, J. He, *Mater. Futures* **2022**, *1*, 025302.
[32] L. Zhang, L. Jin, B. Liu, J. He, *Front. Chem.* **2019**, *7*.
[33] B. Liu, Z. Luo, A. Federico, W. Song, S. L. Suib, J. He, *Chem. Mater.* **2015**, *27*, 6173–6176.
[34] B. Liu, M. Louis, L. Jin, G. Li, J. He, *Chem. Eur. J.* **2018**, *24*, 9651–9657.
[35] M. C. Biesinger, L. W. M. Lau, A. R. Gerson, R. S. C. Smart, *Appl. Surf. Sci.* **2010**, *257*, 887–898.
[36] G. U. Kulkarni, C. N. R. Rao, *Top. Catal.* **2003**, *22*, 183–189.
[37] W.-L. Dai, Q. Sun, J.-F. Deng, D. Wu, Y.-H. Sun, *Appl. Surf. Sci.* **2001**, *177*, 172–179.
[38] H. Zhou, X. Yang, L. Li, X. Liu, Y. Huang, X. Pan, A. Wang, J. Li, T. Zhang, *ACS Catal.* **2016**, *6*, 1054–1061.
[39] F. Jiang, Y. Yang, L. Wang, Y. Li, Z. Fang, Y. Xu, B. Liu, X. Liu, *Catal. Sci. Technol.* **2022**, *12*, 551–564.
[40] S. Velu, K. Suzuki, M. Vijayaraj, S. Barman, C. S. Gopinath, *Appl. Catal. B* **2005**, *55*, 287–299.
[41] C. Baltes, S. Vukojević, F. Schüth, *J. Catal.* **2008**, *258*, 334–344.

Manuscript received: August 26, 2023
Revised manuscript received: November 30, 2023
Accepted manuscript online: November 30, 2023
Version of record online: December 20, 2023